



# Simulation of pressure- and tube-tooling wire-coating flows through distributed computation

A. Baloch, H. Matallah, V. Ngamaramvaranggul  
and M.F. Webster

*Institute of Non-Newtonian Fluid Mechanics,  
Department of Computer Science, University of Wales, Swansea, UK*

**Keywords** *Finite element method, Viscous flows, Parallel computing*

**Abstract** *This article focuses on the comparative study of annular wire-coating flows with polymer melt materials. Different process designs are considered of pressure- and tube-tooling, complementing earlier studies on individual designs. A novel mass-balance free-surface location technique is proposed. The polymeric materials are represented via shear-thinning, differential viscoelastic constitutive models, taken of exponential Phan-Thien/Tanner form. Simulations are conducted for these industrial problems through distributed parallel computation, using a semi-implicit time-stepping Taylor-Galerkin/pressure-correction algorithm. On typical field results and by comparing short-against full-die pressure-tooling solutions, shear-rates are observed to increase ten fold, while strain rates increase one hundred times. Tube-tooling shear and extension-rates are one quarter of those for pressure-tooling. These findings across design options, have considerable bearing on the appropriateness of choice for the respective process involved. Parallel finite element results are generated on a homogeneous network of Intel-chip workstations, running PVM (Parallel Virtual Machine) protocol over a Solaris operating system. Parallel timings yield practically ideal linear speed-up over the set number of processors.*

## 1. Introduction

A number of highly viscoelastic, complex extrusion flows are investigated, commonly associated with the coatings of glass rovings, fibre-optic cables, wire and cable manufacturing processes. Three flow problems are considered, die swell/drag flow (short-die pressure-tooling), full pressure-tooling, and tube-tooling flow. The first two cases are suitable for simulating industrial narrow-bore wire-coating processes. Tube-tooling deals with thicker (wide-bore) wire-coating processes. To provide realistic flow representation for the polymer melt materials used in practice, the specific choice is made of a viscoelastic constitutive model to support shear-thinning and strain-softening behaviour. To this end, an exponential Phan-Thien/Tanner (EPTT) model is selected, flows are computed in a two-dimensional annular coordinate system



---

under creeping flow conditions, and a parallelised version of a semi-implicit time-marching finite element scheme is used, Taylor-Galerkin/pressure-correction (TGPC).

Wire-coating has been studied extensively in experimental and computational form over recent years, see Ngamaramvarangul and Webster (2002) for review. Most studies concentrate on the pressure-tooling design. Modelling assumptions commonly include isothermal flow conditions, incompressibility of the coating flow (Chung, 1986), concentricity of the wire (Tadmor and Bird, 1974), and wire speeds ranging up to one meter per second (Mutlu *et al.*, 1998a). Wire-coating, in the pressure-tooling context, constitutes a process of two flow regimes: a shear dominated flow within an annular die, and an extension-dominated flow along the wire-coating region beyond the die. Injection of the molten polymer into the tooling die establishes a pressure-driven flow. Contact between the molten plastic tube and the wire is made within the die for pressure-tooling, where the travelling wire induces a drag flow, drawing out the polymer melt to form a sheath around the cable. Unique to tube-tooling design is the dependency upon the effects of draw-down beyond the die. Coating production lines for narrow-bore wire use relatively high speeds, around one meter per second, and the deposition of the fluid on a rigid moving wire is treated as a free surface problem.

Recent attention by a number of authors has focused on the simulation of pressure-tooling flow for viscous fluids, such as those of Caswell and Tanner (1978); Pittman and Rashid (1986); Mitsoulis (1986); Mitsoulis *et al.* (1988) and Wagner and Mitsoulis (1985). Their work dealt mainly with shear flow under both isothermal and non-isothermal conditions. Molten polymers have been noted to exhibit highly elastic behaviour when subject to large deformation (Matallah *et al.*, 2001). Only recently, numerical techniques have proven capable of reaching solutions for sufficiently high and relevant levels of elasticity. Many attempts involving either lubrication or inelastic approximations have been conducted to address these shortcomings (Caswell and Tanner, 1978; Mitsoulis *et al.*, 1988; Han and Rao, 1978). With finite elements (FE) Mitsoulis (1986) studied the wire-coating flow of power-law and Newtonian fluids. Mitsoulis concluded that the inclusion of shear-thinning reduced the levels of die-swell at the die-exit, as well as the recirculation that occurred within the die. In a subsequent article, Mitsoulis *et al.* (1988) provided a detailed investigation into high-speed industrial wire-coating. Two flow formulations were used; a planar FE analysis for non-isothermal flows, and a lubrication approximation for isothermal, power-law fluids. Results corroborated the experimental findings of Haas and Skewis (1974).

The inadequacy of inelastic modelling was made apparent by (Binding *et al.*, 1996), rediscrepancies in stress and pressure drop. To predict residual stressing within the melt coating, a viscoelastic analysis was recommended to account for the influence of short residence times of the particles within the flow. Hence,

we have adopted differential viscoelastic models, to predict stress development, using state-of-the-art FE techniques to reach the high deformation rates encountered and associated high Weissenberg numbers,  $O(10^4)$ . For tube-tooling flows and fixed free-surface estimation, we have conducted single-mode PTT (Phan-Thien/Tanner) simulations in Mutlu *et al.* (1998a); Mutlu *et al.* (1998b) and Matallah *et al.* (2001). Tube-tooling was analysed in sections in Mutlu *et al.* (1998a), isolating draw-down flow and studying the effects of stress pre-history and various boundary conditions. This led to a further study (Mutlu *et al.*, 1998b) on coupled and decoupled solution procedures for a range of model fluids, approaching those of industrial relevance. In Matallah *et al.* (2001), single-mode calculations were compared to those of multi-mode type for LDPE and HDPE grade polymers. The multi-mode computations revealed the dominant modes of most significance to the process and gave insight as to the levels of residual stress in the resultant coatings. Further work on multi-mode modelling of Matallah *et al.* (2000), emphasised the influence of die-design on optimal process setting. Three, as opposed to seven modes, were found adequate to sufficiently describe the flow. The draw-down residence time, which dictates the dominance of certain modes within the relaxation time spectrum, was found to be a major factor to influence the decay of residual stressing in the coating.

With specific attention paid to slip for viscous flows, a semi-implicit Taylor-Galerkin/pressure-correction procedure was used by the present authors (Ngamaramvaranggul and Webster, 2000a) for pressure-tooling and tube-tooling. There, the influence of slip onset, as opposed to no-slip conditions within the die, was examined. Tracking free surfaces, our earlier work on model problems addressed stick-slip and die-swell flows, see Ngamaramvaranggul and Webster (2000b); Ngamaramvaranggul and Webster (2001). In a recent article for pressure-tooling (Ngamaramvaranggul and Webster, 2002), the influence of material rheology was investigated on free-surface flow, whilst tube-tooling was the subject in Matallah *et al.* (2001). The present analysis extends upon this work, contrasting comparative designs via a distributed parallel implementation. The computational efficiency over various processor-cluster sizes is of particular interest. Distributed computations are performed over homogeneous network clusters of Intel-chip workstations, running a Solaris Operating System. In this respect, our earlier experience with parallelisation for large, yet model problems (Baloch *et al.*, 2000), is taken into the industrial processing realm. There, Parallel Virtual Machine (PVM) message passing libraries were used over heterogeneous clusters, comprising of DEC-alpha, Intel-Solaris and AMD-K7 (Athlon) Linux processors.

The outline of the current paper is as follows. First, the governing equations are described, followed by the rheological behaviour of the PTT model. In section 4, the three different problems are specified. This is followed, by an outline to the parallel TGPC numerical method employed for the simulations.

The results of the simulations are presented in section 6 and some conclusions are drawn in section 7.

## 2. Governing equations

Isothermal flow of incompressible viscoelastic fluid can be modelled through a system comprising of the generalised momentum transport, conservation of mass and viscoelastic stress constitutive equations. The problems in this study are modeled as annular and two-dimensional. In the absence of body forces, such a system can be represented in the form:

$$\nabla \cdot \mathbf{v} = 0, \quad (1)$$

$$\rho \frac{\partial \mathbf{v}}{\partial t} = \nabla \cdot \boldsymbol{\sigma} - \rho \mathbf{v} \cdot \nabla \mathbf{v}. \quad (2)$$

Here,  $\mathbf{v}$  is the fluid velocity vector field,  $\boldsymbol{\sigma}$  is the Cauchy stress tensor,  $\rho$  is the fluid density,  $t$  represents time, and divergence and gradient operations are implied via  $\nabla$ . The Cauchy stress tensor can be expressed in the form:

$$\boldsymbol{\sigma} = -p\boldsymbol{\delta} + \mathbf{T}_e,$$

where  $p$  is the isotropic fluid pressure,  $\boldsymbol{\delta}$  is the Kronecker delta tensor, and  $\mathbf{T}_e$  is the stress tensor. For viscoelastic flows, stress  $\mathbf{T}_e$  can be decomposed into solvent and polymeric contributions,

$$\mathbf{T}_e = \boldsymbol{\tau} + 2\mu_2 \mathbf{d},$$

with tensors,  $\boldsymbol{\tau}$ , the elastic extra-stress and rate-of-strain  $\mathbf{d} = 0.5[\nabla \mathbf{v} + (\nabla \mathbf{v})^\dagger]$  (superscript  $\dagger$  denotes a matrix transpose).  $\mu_2$  is a solvent and  $\mu_1$  a polymeric solute viscosity, such that  $\mu = \mu_1 + \mu_2$ . The particular choice of constitutive model is that of Phan-Thien and Tanner (1977); Phan-Thien (1978), in exponential form (EPPT). In contrast to models, such as constant shear viscosity Oldroyd-B, this EPPT version supports shear-thinning and finite extensional viscosity behaviour. The constitutive equations for the extra-stress of the EPTT model is expressed as:

$$\lambda_1 \frac{\partial \boldsymbol{\tau}}{\partial t} = 2\mu_1 \mathbf{d} + f\boldsymbol{\tau} - \lambda_1 \{ \boldsymbol{\tau} \cdot \nabla \mathbf{v} + (\nabla \mathbf{v})^\dagger \cdot \boldsymbol{\tau} - \mathbf{v} \cdot \nabla \boldsymbol{\tau} \}, \quad (3)$$

with an averaged relaxation time  $\lambda_1$  and function  $f$ , defined in terms of trace of stress, trace ( $\boldsymbol{\tau}$ ), as:

$$f = \exp \left[ \frac{\epsilon \lambda_1}{\mu_1} \text{trace}(\boldsymbol{\tau}) \right].$$

The material parameters that control shear and elongational properties of the fluid are  $\epsilon$  and  $\mu_1$ , respectively. These may be evaluated by fitting to the

experimental data (Matallah *et al.*, 2001; Matallah *et al.*, 2000). When  $\varepsilon$  vanishes, the Oldroyd-B model is recovered and  $f = 1$ .

We find it convenient to express the governing equations in non-dimensional form, by defining corresponding scales of characteristic length  $R$ , taken as coating length (Figures 2–4), and wire-speed as characteristic velocity scale,  $V$ . Then, stress and pressure are scaled by a factor of  $\mu V/R$ , and time by  $R/V$ . There are two non-dimensional group numbers of relevance, Weissenberg number  $We = V\lambda_1/R$  and Reynolds number  $Re = \rho VR/\mu$ .

### 3. Shear and elongational behaviour of EPTT

Many common non-Newtonian fluids exhibit non-constant viscosity behaviour. So, for example, such materials may display shear-thinning, where the viscosity is a decreasing function of increasing shear rate as illustrated in Figures 1a in pure shear. Figure 1b reflects a similar plot, demonstrating the functional dependence of viscosity under increasing strain-rate in pure uniaxial extension. This is termed the elongational or extensional viscosity behaviour. The merits of the PTT model over the Maxwell model are highlighted by Phan-Thien and Tanner (1992), noting that, the Maxwellian elongational viscosity is singular at finite strain rates. The shear and extensional viscosity functions,  $\mu_s$  and  $\mu_e$ , of the PTT model variants may be expressed as a function of  $f$  itself, taken of exponential form as above, via

$$\mu_s(\dot{\gamma}) = \mu_2 + \frac{\mu_1}{f}, \quad (4)$$

and

$$\mu_e(\dot{\varepsilon}) = 3\mu_2 + \frac{2\mu_1}{f - 2\lambda_1\dot{\varepsilon}} + \frac{\mu}{f + \lambda_1\dot{\varepsilon}}. \quad (5)$$

Under general flow conditions, there is need to record generalized shear and strain-rates, that are defined via flow invariants as, respectively:

$$\dot{\gamma} = 2\sqrt{\Pi_d}, \quad \dot{\varepsilon} = 3\frac{\text{III}_d}{\Pi_d}, \quad (6)$$

where  $\Pi_d$  and  $\text{III}_d$  are the second and third invariants of the rate of strain tensor  $\mathbf{d}$ . Such quantities are represented as

$$\Pi_d = \frac{1}{2}\text{trace}(\mathbf{d}) = \frac{1}{2}\left\{ \left(\frac{\partial v_r}{\partial r}\right)^2 + \left(\frac{\partial v_z}{\partial z}\right)^2 + \left(\frac{v_r}{r}\right)^2 + \frac{1}{2}\left(\frac{\partial v_r}{\partial z} + \frac{\partial v_z}{\partial r}\right)^2 \right\}, \quad (7)$$

$$\text{III}_d = \det(\mathbf{d}) = \frac{v_r}{r}\left\{ \frac{\partial v_r}{\partial r} \frac{\partial v_z}{\partial z} - \frac{1}{4}\left(\frac{\partial v_r}{\partial z} + \frac{\partial v_z}{\partial r}\right)^2 \right\}. \quad (8)$$

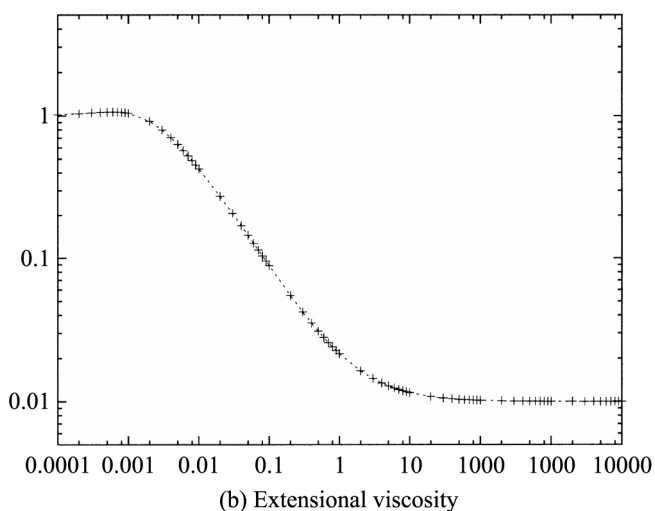
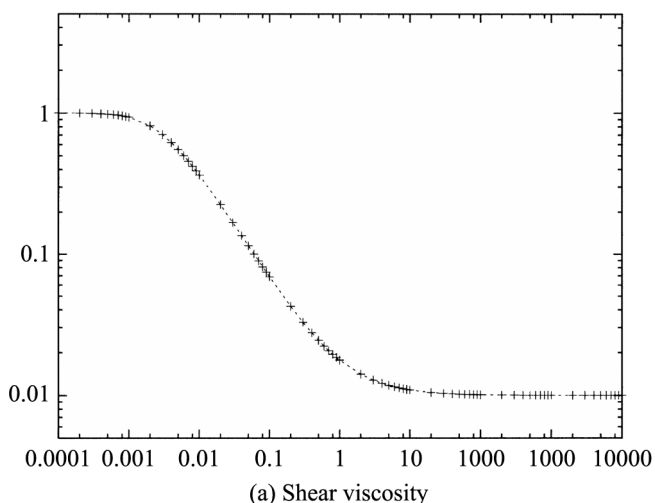
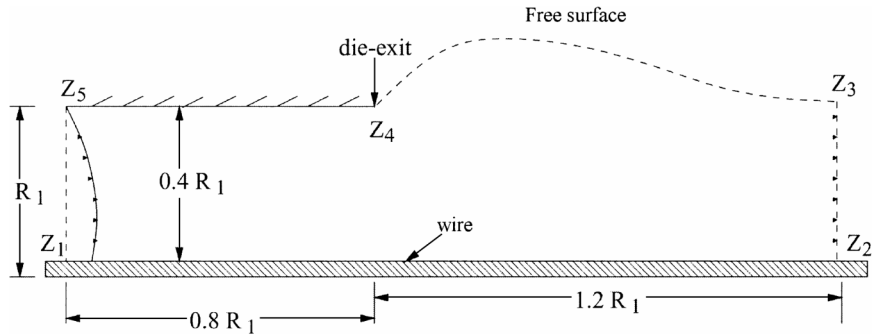
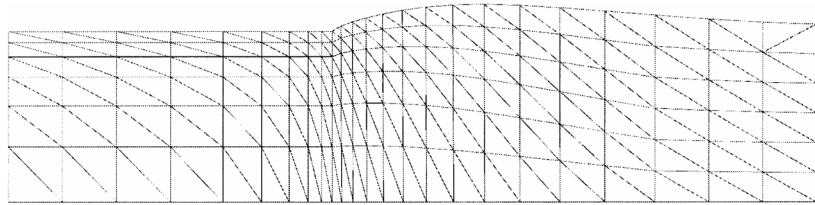


**Figure 1.**  
EPTT model

In pure shear,  $\mu_s$  varies with  $\epsilon$ ,  $\mu_1$ , and  $\lambda_1$ . The effect of elevating  $\mu_1$  from levels of 0.88 to 0.99 and 0.95 reduces the second Newtonian plateau level from  $0(10^{-1})$  to  $0(10^{-2})$  and below. Here  $\mu_1 = 0.99$  solute fraction is taken as suitable. Shifting of  $\lambda_1$ , (via  $We$ ) from unity to  $0(10)$  and  $0(10^2)$ , translates  $\mu_s$  in a constant shift fashion. The larger  $\lambda_1$ , the earlier the departure occurs from the first Newtonian plateau. Current material and process settings suggest  $\lambda_1$  of  $0(1s)$  is a reasonable choice, so that  $We = 200$ . With selection of  $\mu_1 = 0.99$  and  $We = 200$ , the influence of the  $\epsilon$ -parameter choice is relatively minor.

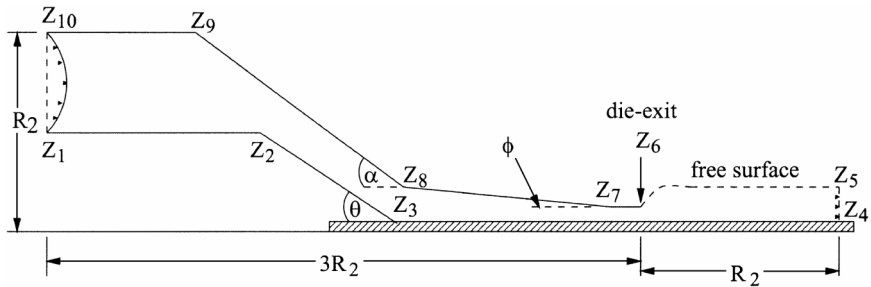


(a) schema

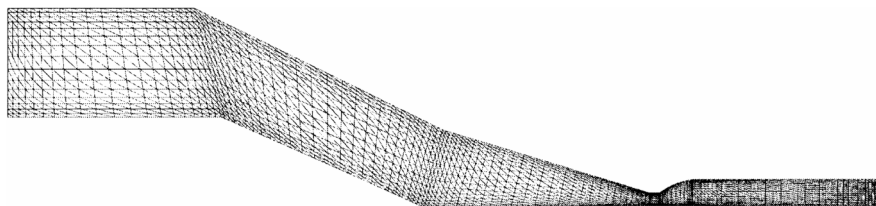


(b) mesh pattern, 6x24 elements

**Figure 2.**  
Short-die pressure-  
tooling



(a) Pressure-tooling: schema



(b) Pressure tooling: mesh pattern, 15x127 elements

**Figure 3.**  
Full-die pressure-  
tooling

Increasing  $\epsilon$  from 0.1 to 0(1) slightly retards the  $\mu_s$  pattern, so that earlier departure from the first Newtonian plateau occurs. Here,  $\epsilon$  of unity is selected.

In steady uniaxial extension,  $\mu_e$  follows the behavioural trends of  $\mu_s$  for both  $We$  and  $\mu_1$  parameters. Distinction may be found via the  $\epsilon$ -parameter. Taking the tuple setting  $(\mu_1, We) = (0.99, 200)$ , for  $0.1 \leq \epsilon \leq 0.5$ , reflects strain-hardening at low strain rates prior to softening at rates above  $10^{-2}$ . Only softening is apparent for  $\epsilon \sim 0(1)$ . The EPTT (1,0.99,200) model demonstrates the desired viscometric functional behaviour, shear-thinning and strain-softening, within the deformation rate ranges of dominant interest for the wire-coating process, as one might typically encounter, say, for an LDPE grade polymer at 230°C. As a consequence of these viscometric functions, we observe later in the actual flows of current interest, that maximum shear-rates may rise to  $O(10^2)$  units, whilst strain-rates reach  $O(10^1)$ . This, in turn, implies that second Newtonian plateaus will be reached *in-situ*.

#### 4. Specification of problems

This paper deals with the study of three types of flow: die swell/drag flow (short-die tooling), full-die pressure-tooling flow, and tube-tooling flow.

##### 4.1 Die-swell/drag flow

This annular problem illustrates the progressive effects of an imposed drag flow from the travelling wire on both the classic die swell problem (within the free jet-flow region) and stick-slip flow (see Figure 2). Mesh refinement considerations follow our previous studies (Ngamaramvaranggul and Webster, 2002; Ngamaramvaranggul and Webster, 2000b; Ngamaramvaranggul and Webster, 2001), where the fine mesh of Figure 2b is found suitable. The flowrate through the die is fixed by the fully-developed annular inlet flow profile under pressure-driven conditions. No-slip conditions are applied at the die wall boundaries. The wire and inlet channel radii comprise the characteristic length, while characteristic velocity is directly related to the constant wire-speed at the lower boundary of the domain. The rapid reduction in traction at the free jet surface gives rise to the fully-developed plug flow at the domain outflow.

##### 4.2 Pressure-tooling

Pressure-tooling flow is an extension to the previous die-swell/drag flow study, the domain of which is specified in Figure 3a. This domain contains an initial short-die flow zone within the land region of the die ( $z_6, z_7$ ), followed by a jet flow region at the die exit. The traveling wire within the die, moving at a fixed speed, first makes contact with the pressure-driven annular flow at  $z_3$  station. The influence of the wire on the polymer melt at this boundary region is referred to in Ngamaramvaranggul and Webster (2002); Binding *et al.* (1996); Ngamaramvaranggul and Webster (2000a). Flow within the die is restrained by no-slip boundary conditions at the die walls. The swelling effects observed in

the jet flow region are caused by the sudden drop to atmospheric pressure, combined with the immediate lack of traction. This swell, in the extruded polymer, levels out to a fully-developed plug flow, by the time it reaches the end of the pressure-tooling domain. The biased fine mesh of Figure 3b is employed, for further details see our prior study (Ngamaramvaranggul and Webster, 2002).

4.3 Tube-tooling

A schematic illustration of the full-die tube-tooling domain is shown in Figure 4a. This was computed upon with the fine mesh of Figure 4b. Problem dimensions are largely in common with the full pressure-tooling specification. So, for example, the lower and upper die wall converging angles are  $30^\circ$  and  $17^\circ$ , at positions  $z_{10}$  and  $z_3$ , respectively. No-slip die-wall boundary conditions apply throughout the die. In the final draw-down region ( $z_4z_5$  and  $z_8z_9$ ), free surface conditions apply. For tube-tooling, the wire makes contact with the polymer melt at the end of the draw-down region  $z_5$ , with the coating length upon the wire being taken as the characteristic length  $R_2$ . As for pressure-tooling, the wire dimensions, inlet hydraulic radius ( $R_2$ ), and total die length ( $3R_2$ ), again apply in this example. In our previous investigations (Ngamaramvaranggul and Webster, 2002; Ngamaramvaranggul and Webster, 2001), we focused upon mesh convergence studies. Here, numerical solutions are generated on fine meshes only, the detailed statistics of which are recorded in Table I for all three problems, inclusive of degrees of freedom (DOF), for Newtonian ( $N$ ) models and viscoelastic ( $V$ ) models.

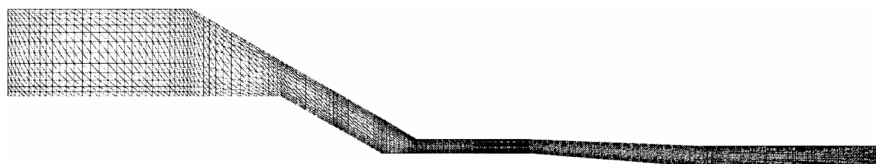
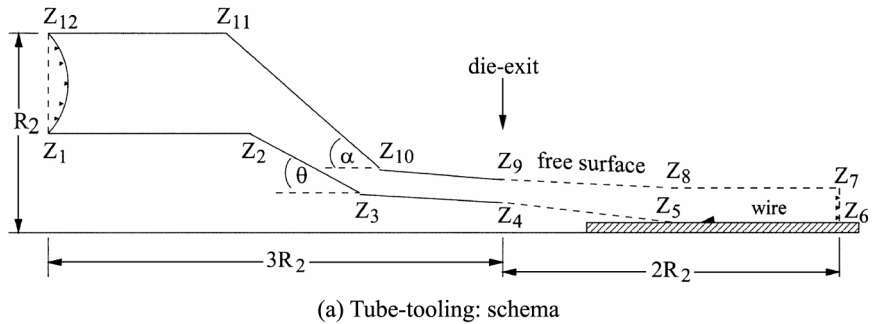


Figure 4.  
Full-die tube-tooling

## 5. Numerical scheme

### 5.1 Sequential Taylor-Galerkin algorithm

A time-marching finite element algorithm is employed in this investigation to compute steady viscoelastic solution through a semi-implicit Taylor-Petrov-Galerkin/pressure-correction scheme (Townsend and Webster, 1987; Hawken *et al.*, 1990; Carew *et al.*, 1993; Baloch and Webster, 1995; Baloch *et al.*, 1998; Matallah *et al.*, 1998), based on a fractional-step formulation. This involves discretisation for equations (1–3), first in the temporal domain, adopting a Taylor series expansion in time and a pressure-correction operator-split, to build a second-order time-stepping scheme. Spatial discretisation is achieved via Galerkin approximation for momentum and Petrov-Galerkin for the constitutive equations. The finite element basis functions employed are quadratic for velocities and stress, and linear for pressure, defined over two-dimensional triangular elements. Galerkin integrals are evaluated by a seven point Gauss quadrature rule. The time-stepping scheme includes a semi-implicit treatment for the momentum equation to avoid restrictive viscous stability constraints. Solution of each fractional-staged equation is accomplished via an iterative solver. That is, with the exception of the temporal pressure-difference Poisson equation, which is solved through a direct Choleski procedure. The semi-implicit Taylor-Galerkin/pressure-correction method may be presented in semi-discrete temporal format as:

Stage 1a:

$$\frac{2Re}{\Delta t}(\mathbf{v}^{n+\frac{1}{2}} - \mathbf{v}^n) = [\nabla \cdot (2\mu_2 \mathbf{d} + \boldsymbol{\tau}) - Re \mathbf{v} \cdot \nabla \mathbf{v} - \nabla p]^n + \nabla \cdot \mu_2 (d^{n+\frac{1}{2}} - d^n),$$

$$\frac{2We}{\Delta t}(\boldsymbol{\tau}^{n+\frac{1}{2}} - \boldsymbol{\tau}^n) = 2\mu_1 \mathbf{d} - f\boldsymbol{\tau} - We[\mathbf{v} \cdot \nabla \boldsymbol{\tau} - \nabla \mathbf{v} \cdot \boldsymbol{\tau} - (\nabla \mathbf{v} \cdot \boldsymbol{\tau})^\dagger]^n.$$

Stage 1b:

$$\frac{Re}{\Delta t}(v^* - v^n) = [\nabla \cdot (2\mu_2 \mathbf{d} - \nabla p)^n + [\nabla \cdot \boldsymbol{\tau} - Re \mathbf{v} \cdot \nabla \mathbf{v}]^{n+\frac{1}{2}} + \nabla \cdot \mu_2 (d^* - d^n),$$

$$\frac{We}{\Delta t}(\boldsymbol{\tau}^{n+\frac{1}{2}} - \boldsymbol{\tau}^n) = 2\mu_1 \mathbf{d} - f\boldsymbol{\tau} - We[\mathbf{v} \cdot \nabla \boldsymbol{\tau} - \nabla \mathbf{v} \cdot \boldsymbol{\tau} - (\nabla \mathbf{v} \cdot \boldsymbol{\tau})^\dagger]^{n+\frac{1}{2}}.$$

Meshes	Elements	Nodes	DOF(N)	DOF(V)
Short-die	288	377	929	2437
Pressure-tooling	3810	7905	17858	49478
Tube-tooling	4714	9755	22031	61051

**Table I.**  
Finite element mesh  
data

Stage 2:

$$\frac{\Delta t}{2} \nabla^2 (p^{n+1} - p^n) = \text{Re} \nabla \cdot v^*$$

Stage 3:

$$\frac{2\text{Re}}{\Delta t} (v^{n+1} - v^*) = -\nabla(p^{n+1} - p^n).$$

Here,  $n$  is the time step number and  $v^*$  is a non-solenoidal vector field. The velocity and stress components of Stage 1a are taken for a half time step (i.e.,  $n + 1/2$ ), while at Stage 1b, the  $v^*$  velocities and stresses are computed over a full time step ( $n + 1$ ). In combination, Stage 1 constitutes a predictor-corrector doublet, performed once per time-step. This concludes derivation of stress components for a complete time step. Pressure differences over this period are calculated from the Poisson equation (Stage 2), depending upon the intermediate vector field  $v^*$ . Solution of this Poisson equation yields the solenoidal velocity over a full time step, as shown in Stage 3 (see Townsend and Webster (1987); Hawken *et al.* (1990)). Free-surface reassessment is conducted at a fourth stage (see on). Recovery of velocity gradients within the constitutive equation further enhances stability of the system, along with streamline-upwind Petrov-Galerkin weighting. Determination of time step (typically  $O(10^{-3})$ ) is made on the basis of a Courant stability constraint.

### 5.2 Parallel Taylor-Galerkin algorithm

The semi-implicit time-stepping TGPC algorithm is parallelised as follows. Each of the individual fractional-stage phases of the algorithm is parallelised within a single time-step loop. This implies operations of gather and scatter of data, pre- and post- each phase, respectively. In such a manner, the combined problem is split into associated sub-problems relating to each subdomain. We relate such operations with message passing between master and slave processors, achieved via PVM *send* and *receive* communication commands. This is a crucial issue to ensure correct system configuration and network communication. This slave processors solve subdomain problems, whilst the master processor resolves the interface problem and controls master-slave communication (Grant *et al.*, 1998).

Of the various fractional-stages, the pressure equation step is the only one that is conducted through a direct solution procedure (Choleski), involving the explicit parallel construction and solution of a matrix problem. Remaining stages are associated with an iterative solution procedure (Jacobi). It is upon this basis that the exceptional parallel performance characteristics are achieved. The complete detail behind the parallelisation of the TGPC and these two algebraic solution procedures is provided in Grant *et al.* (1998). Briefly, both necessitate an assembly and solution phase, involving finite element loop

construction of right-hand-side vectors and matrix components. For Choleski, the matrix components must be stored. Fortunately, this is manageable even for large problems, as the pressure variable in question is of scalar form on the field.

Solution phases radically differ between iterative and direct procedures. The iterative solution phase is nodally-based. Each sub-problem on a slave processor, first computes contributions for the boundary (interfacing) nodes, so that their result may be communicated to the master processor directly, whilst the computation for interior sub-domain nodes is completed. This enables effective masking of communication. The master processor must then process the combined domain contributions for the *interfacing nodes*, as well as performing system synchronisation and intercommunication processor control. Utilising an iteration number  $r$ , acceleration factor  $\omega$ , right-hand side vector  $\mathbf{b}$ , iteration sub-domain vector  $\mathbf{X}_{P_i}$ , system (mass) matrix  $\mathbf{M}_{fe}$  and diagonal matrix  $\mathbf{M}_d$ , the parallel finite element Jacobi iteration may be expressed in concise notational form, as

$$\text{par} \begin{bmatrix} X_{P_1} \\ \dots \\ X_{P_2} \\ \dots \\ X_{P_3} \\ \dots \\ \vdots \\ \dots \\ X_{P_n} \end{bmatrix}^{r+1} = (I - \omega M_d^{-1} M_{fe}) \begin{bmatrix} X_P \\ \dots \\ X_P \\ \dots \\ X_{P_3} \\ \dots \\ \vdots \\ \dots \\ X_{P_n} \end{bmatrix}^r + \omega M_d^{-1} [\mathbf{b}]_{\text{nodes}}$$

The mass-matrix ( $\mathbf{M}_{fe}$ ) is based on quadratic finite element functions, its diagonalised form ( $\mathbf{M}_d$ ) is one of absolute row-sum, and the iterative acceleration parameter  $\omega$  may be selected to suit (often simply taken as unity). System matrices are referenced and evaluated at the element level only, so that a complete system is never stored. A single iteration sweep of this sort will maintain integrity levels of the data re-synchronisation. Care likewise must be taken with respect to consistent solution increment tolerance calculations, across individual slave and master processors.

The parallel direct solution phase adopts a Schur-complement approach. This introduces a herring-bone structure to the complete system matrix problem, via the associated nodal numbering on each subdomain and the

interfacing boundary nodes. The parallel herring-bone structure of the Choleski system matrix may be represented as

$$\begin{array}{c}
 \uparrow \\
 \text{par} \\
 \downarrow
 \end{array}
 \left[ \begin{array}{cccccc}
 [P_1] & & & & & [MP_1] \\
 & [P_2] & & & & [MP_2] \\
 & & [P_3] & & & [MP_3] \\
 & & & \ddots & & \cdot \\
 & & & & \ddots & \cdot \\
 & & & & & [P_n] & [MP_n] \\
 [P_1M] & [P_2M] & [P_3M] & & & [P_nM] & [M]
 \end{array} \right]$$

Herring Bone Structure (Schur-complement)

with  $[P_i]$  the subdomain problem for the interior of subdomain  $i$ ,  $[P_iM]$ , the matrix contribution of interior subdomain  $i$  to the boundary-node problem, and  $[M]$  that for the boundary-nodes.

The subdomain problem, for each interior subdomain (on a single slave processor), may be solved in parallel with all others. Finally, the interfacing-node matrix problem is solved, for which all available processors may be used. To date, the size of the interfacing-node matrix problem has been such that a single processor (the master) has been employed to resolve it. In such a fashion, it is possible to render large-scale problems tractable, typically of three-dimensional or viscoelastic form (Grant *et al.*, 1998).

### 5.3 Free-surface procedure

The term die-swell describes the radial increase of the polymer melt in the free-jet flow on exiting the die. It is represented as the swelling ratio ( $\chi = R_j/R$ ), where  $R_j$  is the jet radius and  $R$  is the tube radius. This phenomenon is of considerable significance to some polymer processing operations in industry. For creeping flow, without gravity, and with large surface tension, die swell was defined analytically by Richardson (1970). A number of numerical schemes can be used to calculate die swell. Comparisons in performance between free surface estimation algorithms, utilising finite differences, finite elements, and boundary element methods can be found in Crochet *et al.* (1984) and Tanner (1985). These surveys cover the varying accuracy of the above methods and asymptotic analysis for viscoelastic and Newtonian fluids in axisymmetric and planar die flows. Below we introduce two schemes for the numerical prediction of free surfaces: the streamline prediction method and the mass balance method. These are incorporated into the present algorithm at a fourth terminating stage within the time-step loop.

#### 5.4 Stream-line prediction method

A modified iterative free surface location method was used to determine extrusion profiles. Three boundary conditions are used to describe the free surface, see Crochet *et al.* (1984),

$$v_r n_r + v_z n_z = 0, \quad (9)$$

$$t_r n_r + t_z n_z = S \left( \frac{1}{\rho_1} + \frac{1}{\rho_2} \right), \quad (10)$$

$$t_r n_z - t_z n_r = 0, \quad (11)$$

Where free surface unit normal components are  $(n_r, n_z)$ , curvature radii  $(\rho_1, \rho_2)$ , surface tension coefficient  $S$  (vanishes here), radial and axial velocities  $(v_r, v_z)$  and surface forces normal to the free surface  $(t_r, t_z)$ .

Boundary condition (10) and (11) are used when iteratively modelling the free surface. Condition (9) is then included to define the normal velocity. The upper extruded flow surface can then be obtained for die-swell extrusion. For a tube radius  $R$ , the distance  $r(z)$  of the free surface from the axis of symmetry is represented by:

$$r(z) = R + \int_{z=0}^{\infty} \frac{v_r(z)}{v_z(z)} dz. \quad (12)$$

In order to accurately predict the extrusion shape, Simpsons quadrature rule is used to compute the integral of equation (12).

The procedure of solution is as follows. First, the kinematics for a converged Newtonian solution is used as initial conditions, with a relaxed stress field, and the fixed free-surface problem is solved. Subsequently, the full problem is computed, involving the free surface calculation, where the surface location itself must be determined. Continuation from one particular viscoelastic solution setting to the next is then employed. In some instances, it is stabilising to first enforce vanishing surface extra-stress ( $\tau$  of equation (3)), prior to relaxing such a constraint. To satisfy the zero normal velocity free surface boundary condition and to compensate for the adjustment of the free surface, the velocity solution at the advanced time surface position must be reprojected from the previous surface position.

#### 5.5 Mass balance method

The pressure drop/mass balance method provides an adequate means of correcting the estimation of the free surface position. Such a technique may provide improved solution accuracy and stability over the regular streamline location method. The procedure involves taking, an initial estimate of the free-surface profile for each Weissenberg number. Sampling points for We

begin from the stick-slip region. The final correction stage makes use of the streamline method, to perturb and validate the position of the die swell surface.

By examining the functional dependence of pressure drop ( $\Delta p$ ) in swell ( $\chi$ ) profiles at the centreline, for each  $We$  level, the mass balance scheme relates flow characteristics between the stick-slip to die-swell phases of the problem (akin to an expression of energy balance). By taking into account known swell predictions with sampled pressure drop results, a general relationship may be established between these two scenarios:

$$\chi(z) = \frac{\Delta p(z, We)}{f(We)},$$

By fitting to prior and accepted data (say at low  $We$  levels, from the streamline method), the denominator can be represented by:

$$f(We) = 10.68 - 0.133We - 2.125 We^2.$$

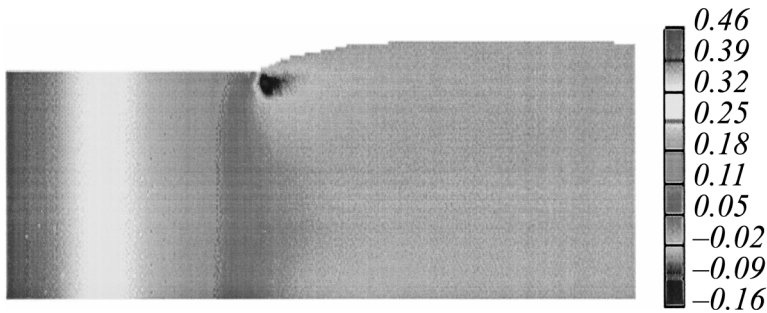
Using this approach, it is possible to derive the approximate swell after pressure drop calculations are made. This process is then implemented within an iterative time-stepping procedure, to obtain a converged solution. Such a strategy is found to be absolutely necessary to achieve converged free-surface solutions at the extreme levels of parameters relevant to industrial processing, notably high  $We$  and low solvent contribution.

## 6. Numerical predictions and discussion

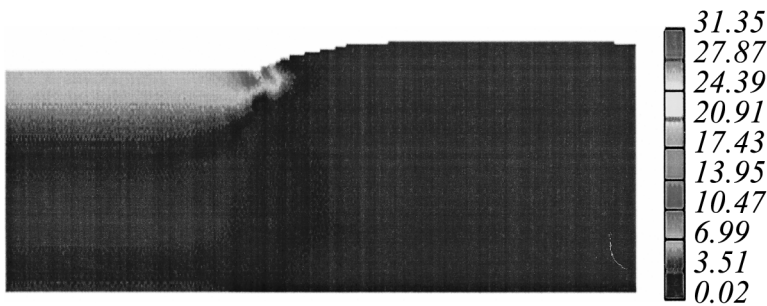
### 6.1 Short-die, pressure-tooling

The solution for short-die pressure-tooling is illustrated through field plots, in terms of pressure, extension rate and shear rate in Figure 5 and stress component contours in Figure 7. The short-die problem, taken on the  $6 \times 24$  element mesh, is idealised flow. It proves useful to encapsulate the essence of pressure-tooling, devoid of the complexity of the full die. In contrast, the full-die study reveals the implications of actual processing conditions.

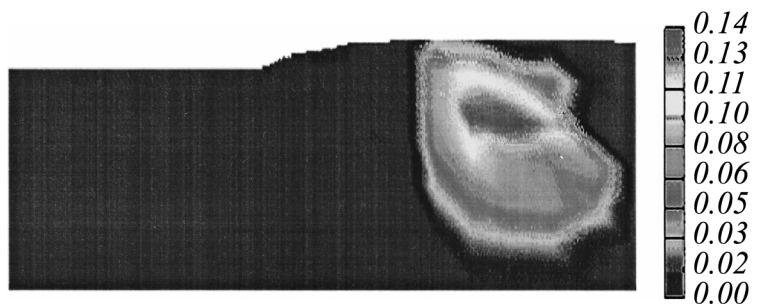
The pressure drop across the flow reaches 0.46 units (relative to ambient pressure), where the die length to exit gap width ratio is of the order 2:1. This drop corresponds to that across the die alone. The minimum pressure arises at the top surface die-exit. The shear rate  $I_2$  is two orders of magnitude larger than the extension rate, peaking with 31.3 units at the top die-exit boundary. Upon entering the jet region, the shear rate rapidly decline and vanishes. The flow profile adjusts from a shear flow within the die to a plug flow in the jet. The flow profiles of Figure 6 reflect this position, with a linear decrease in pressure observed along the wire within the die. Maximum swell within the jet reaches 1.054 units. This would correspond to typical results reported in the literature Mitsoulis (1986); Mitsoulis *et al.* (1988); Wagner and Mitsoulis (1985);



(a) pressure contours



(b)  $I_2$  contours

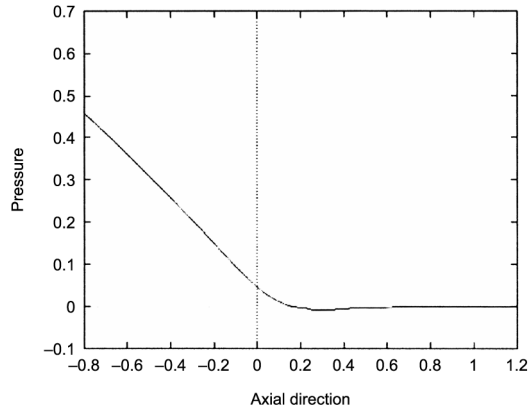


(c)  $\dot{\epsilon}$  contours

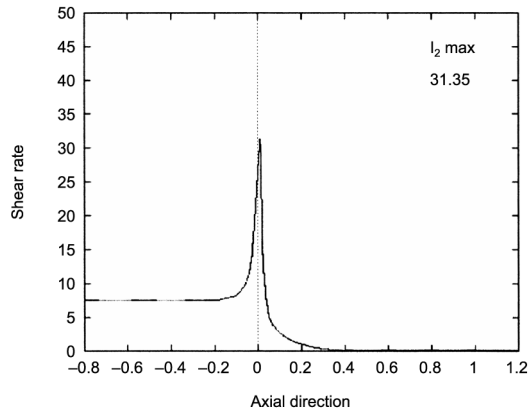
Figure 5.  
Short-die

Ngamaramvaranggul and Webster (2000b); Ngamaramvaranggul and Webster (2001).

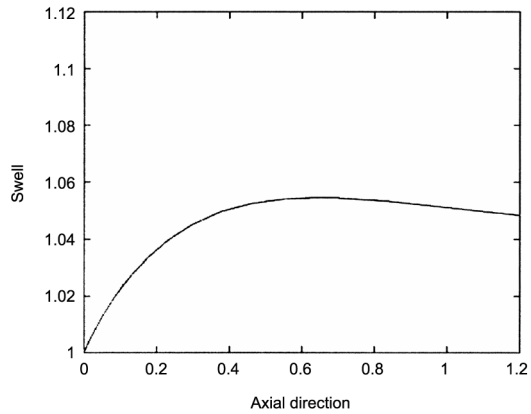
Field plots on the stress components of Figure 7, illustrate the dominance of the axial stress, that in maxima is three times larger than the shear stress and five times larger than the radial stress. The sharp adjustment is noted at die-exit on the top-surface in both shear and axial stress,  $T_{rz}$  and  $T_{zz}$ -profiles of Figure 8 and 9, respectively. Profiles on the wire are relatively smooth, in contrast. We have observed in our earlier work (Ngamaramvaranggul and Webster, 2002), that the strain-softening response of the EPTT model, stabilises



(a) pressure along the wire



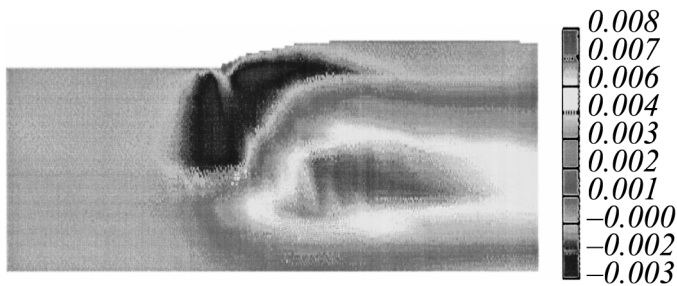
(b)  $I_2$  on top surface



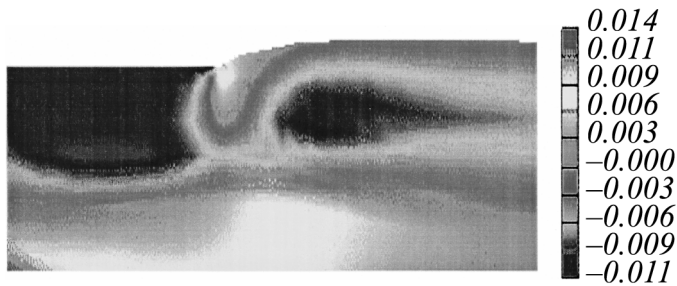
(c) die swell on top free

**Figure 6.** Short-die; (a) pressure along the wire, (b)  $I_2$  on top surface, (c) die swell on top free

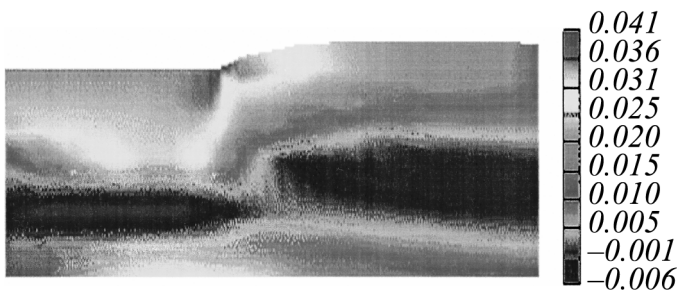
---



(a)  $T_{rr}$  contours



(b)  $T_{rz}$  contours



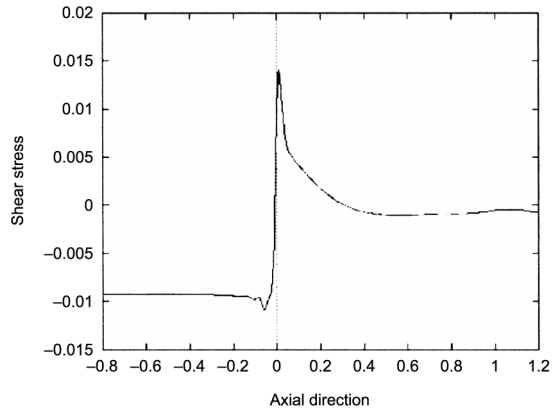
(c)  $T_{zz}$  contours

**Figure 7.**  
Short-die: (a)  $T_{rr}$   
contours, (b)  $T_{rz}$   
contours, (c)  $T_{zz}$  contours

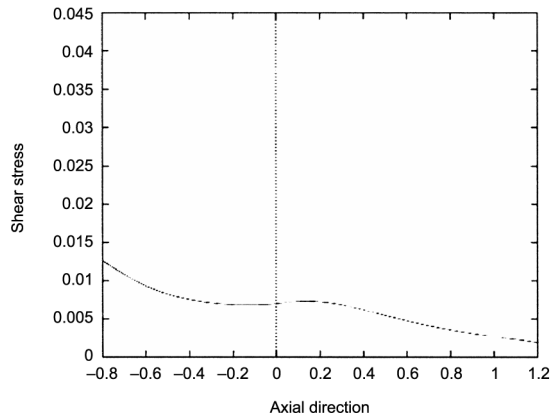
stress profiles. This stands in stark contrast to models that support strain-hardening.

### 6.2 Full-die, pressure-tooling

Following our earlier study on mesh convergence (Ngamaramvaranggul and Webster, 2002), for this problem our results are plotted upon the biased fine mesh of Figure 3b, with identical parameter settings as for the short-die flow. The zonal refinements are outlined in Table II, with greatest density and bias in the land and die-exit regions.



(a) on top surface

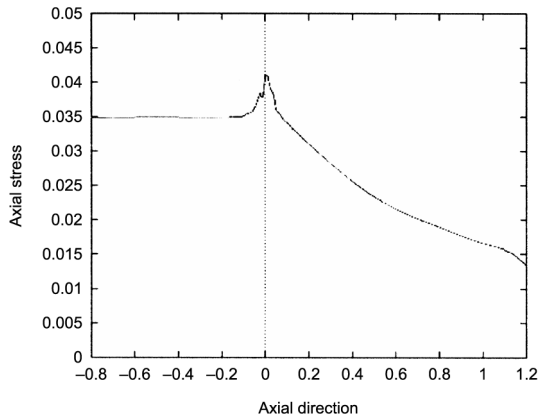


(b) on wire

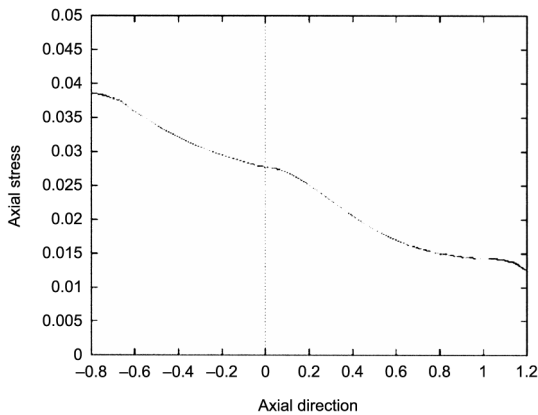
**Figure 8.**  
Short-die:  $T_{rz}$  (a) on top surface, (b) on wire

The filed plots of Figure 10 indicate an intense drop in pressure local to the land region, reaching a maximum pressure drop of 10.1 units. Shear rate,  $I_2$ , also identifies significant shearing over the land region, reaching a peak of 461 units at the die-exit, a fifteen fold increase to that obtained for short-die tooling.

	Sub-region zone	Biased fine mesh
<b>Table II.</b> Full-die pressure-tooling; mesh characteristics, sub-region zones	1. inlet die	$15 \times 20$
	2. converging die	$15 \times 25$
	3. coating region	$15 \times 30$
	4. land region	$15 \times 5$
	5. jet region	$15 \times 47$



(a) on top surface



(b) on wire

**Figure 9.**  
Short-die  $T_{zz}$  (a) on top  
surface, (b) on wire

Strain rates,  $\dot{\epsilon}$ , are an order of magnitude lower than shear rates, and display peaks at melt-wire contact and die-exit. At the melt-wire contact point,  $\dot{\epsilon}$  increases to 8.37 units. A rapid larger rise occurs in the wire-coating section at die-exit. The second peak in  $\dot{\epsilon}$ -profile at the top boundary, characteristic for the full-die, reaches a height of 18.8 units in the post-die exit region.

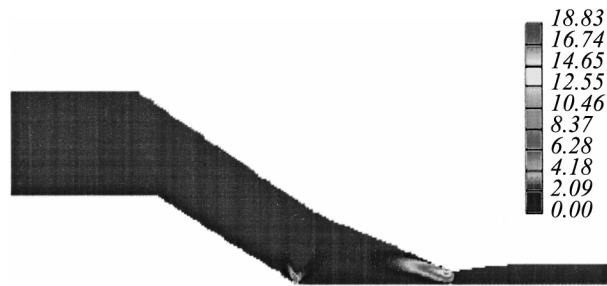
The pressure along the bottom surface corresponds to the line contour plot of Figure 11a. Pressure difference is twenty two times greater for the full case, above short-die pressure-tooling (as compared with Figure 5). Note that, these drops in pressure, essentially correspond to the same flow zone, that is, over the land-region at jet-entry. The die-swell profile along the top free-surface is given in Figure 11b. The swelling ratio is fifteen percent larger than that for short-die pressure-tooling.



(a) pressure contours



(b)  $I_2$  contours

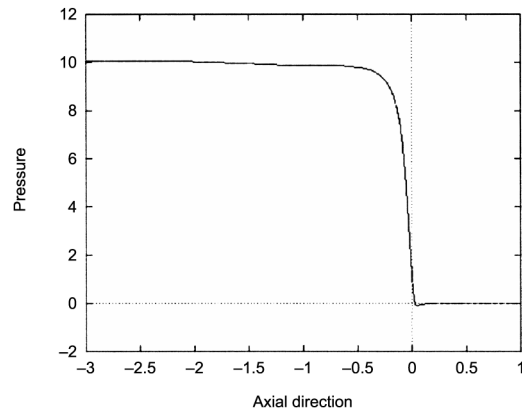


(c)  $\dot{\epsilon}$  contours

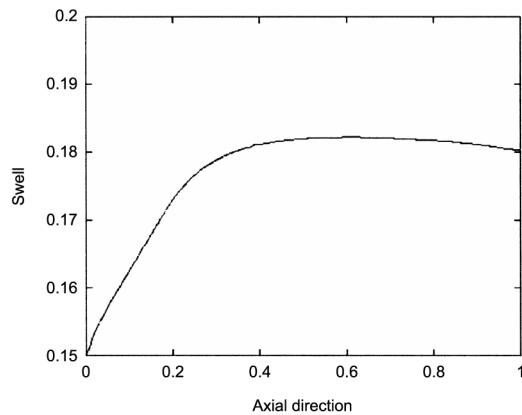
**Figure 10.**  
Full-die pressure-tooling:  
(a) pressure contours,  
(b)  $I_2$  contours, (c)  $\dot{\epsilon}$   
contours

Shear rate profiles, along the top and bottom surfaces, are represented in Figure 12. The top surface  $I_2$  peak of 461.7 units at the die-exit (Figure 12a), is fifteen times greater than that for short-die, pressure-tooling (see Figure 6b). Figure data on  $I_2$  maxima may be found in Table III. Along the bottom surface, the double (sudden shock) peaks of 124 and 140 units of Figure 12b are most prominent. Such peaks do not appear in the short-die case, being a new introduction as a consequence of the full-die and melt-wire contact.

The “shock impact” as the fluid makes contact with the wire is most prominent in the radial, shear and axial stress contour plots of Figure 13.



(a) pressure along the wire

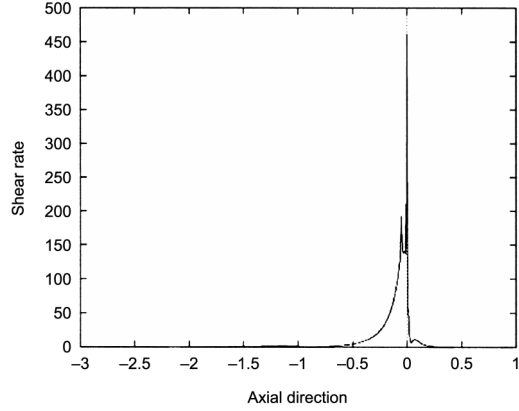


(b) die swell on top free

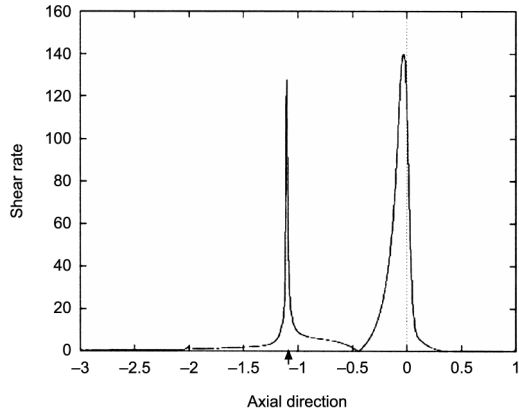
**Figure 11.**  
Full-die pressure-tooling:  
(a) pressure along the  
wire, (b) die swell on top  
free

Nevertheless, stress levels within the die remain small, the greatest axial stress of 0.069 units occurs upon melt-wire contact.

Top-surface stress profiles of Figure 14a and 15a, demonstrate most clearly, the “localised effect” of die-exit point discontinuity. A violent jump in shear stress is observed over the land region. Comparison of stress between full-die and short-die pressure-tooling instances reveals factor increases of 1.8 times in  $T_{rz}$  and 1.7 times in  $T_{zz}$  (Table III). Both shear and axial stress profiles along the bottom wire-surface reveal the influence of the moving-wire on the flow at the melt-wire contact point (axial position  $-1.1$  units). In axial stress of Figure 15, along the *bottom surface*, the characteristic “double peak” profile at the melt-wire contact point and die-exit regions is observed. The axial stress peak at the melt-wire contact point exceeds that at die-exit and is followed by a sharp relaxation on the approach to the land region, upon which a more



(a) on top surface



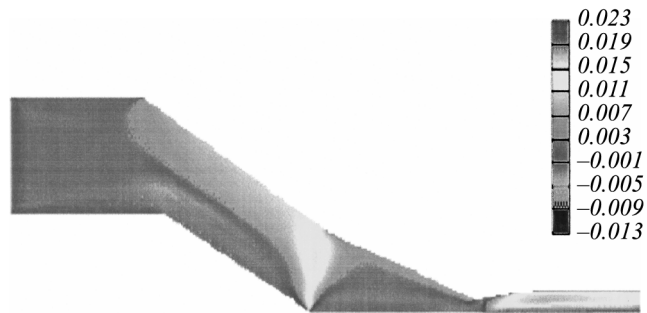
(b) on bottom surface

**Figure 12.**  
Full-die pressure-tooling:  
 $I_2$  (a) on top surface, (b) on  
bottom surface

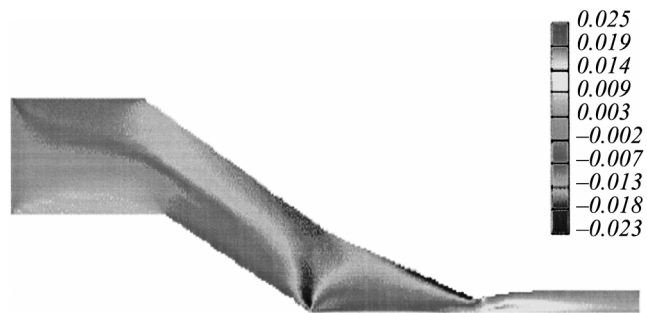
sustained maxima forms. Notably, in the extrudate,  $T_{zz}$  remains positive, and provides some residual stressing to the coating.  $T_{zz}$ -maxima increase only slightly from case to case, with full-case pressure-tooling values being about twice for the short-die instance.

**Table III.**  
EPTT ( $\epsilon = 1$ ,  $\mu_1 =$   
0.99,  $We = 200$ ),  
solution values

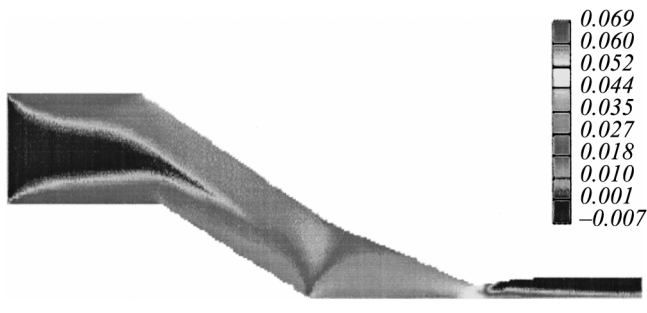
Solution variables	Short-die	Full-die	Tube-tooling
$I_2$ max, Top	31.35	461.7	127.7
$I_2$ max, Bot	–	139.7	144.2
$\dot{\epsilon}$ max	0.144	18.83	4.43
$\Delta p$	0.462	10.18	16.09
$T_{rx}$ max	0.014	0.025	0.024
$T_{zz}$ max	0.041	0.069	0.050
$\chi$	1.054	1.215	–



(a)  $T_{rr}$  contours



(b)  $T_{rz}$  contours

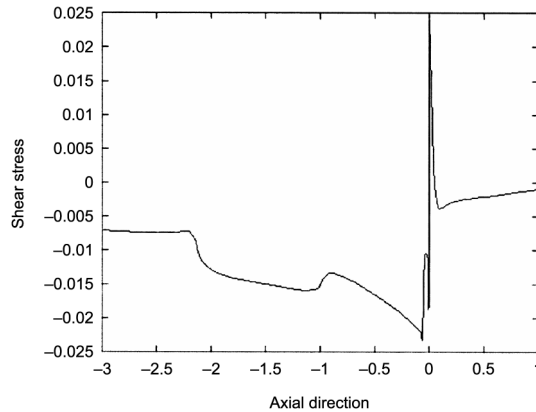


(c)  $T_{zz}$  contours

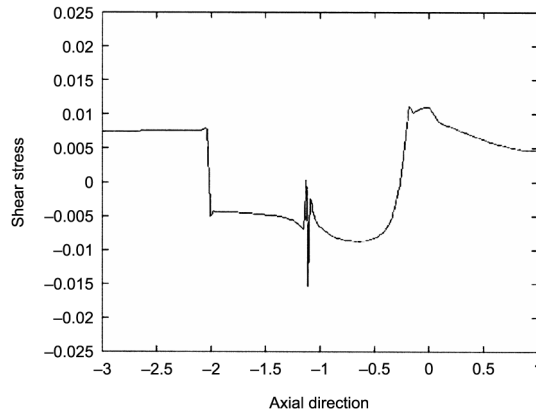
**Figure 13.**  
Full-die pressure-tooling:  
(a)  $T_{rr}$  contours, (b)  $T_{rz}$   
contours, (c)  $T_{zz}$  contours

### 6.3 Tube-tooling

Concerning the tube-tooling problem, our analyses are based on a single refined mesh as displayed in Figure 4b, see Townsend and Webster (1987). Mesh characteristics for each sub-region are provided in Table IV. As displayed in Figure 16a, the pressure-drop is most prominent across the tube-die. At the draw-down and coating regions, the pressure hold to an ambient level. The



(a) on top surface

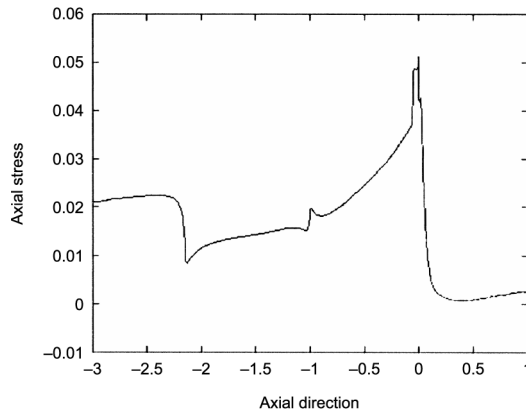


(b) on wire

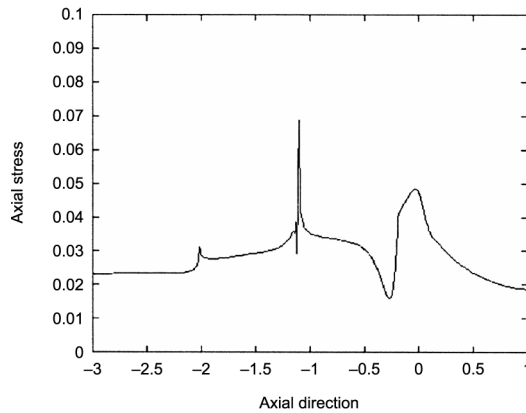
**Figure 14.**  
Full-die pressure-tooling:  
 $T_{rz}$  (a) on top surface,  
(b) on wire

most important rate of change in pressure-drop arises across the land-region, as is true for pressure-tooling. Here, the maximum value is higher, of 16.1 units for tube-tooling compared to 10.2 units for pressure-tooling.

In contrast, shear-rate  $I_2$ , is about a quarter of that corresponding to pressure-tooling. The maximum is 144 units. Again, higher shear-rates are attained in the land-region, see Figure 16b. The remaining regions display smaller shear-rates, so that the shear-viscosity of the polymer melt will be high there. The shear-rate profiles are also displayed in Figure 17b and c, plotted along the top and bottom surfaces in the axial direction. The shear-rates increase across the converging cone, from 0.89 units at the inlet-tube and start of the converging cone to 14.6 units at its end. A sudden rise in shear-rate occurs when the polymer enters the land-region, across which a constant value is generated. Shear-rate maxima are generated at the die-exit, with values of



(a) on top surface



(b) on wire

**Figure 15.**  
Full-die pressure-tooling:  
 $T_{zz}$  a) on top surface,  
b) on wire

144.2 and 127.2 units at the bottom and top surfaces, respectively. Beyond the die-exit entering the draw-down flow, a sharp drop in shear-rate is observed. Similar behaviour is observed in both top and bottom surface shear-rate profiles. There is only a gradual decrease in shear-rate over the draw-down

Sub-region zone	Biased fine mesh
1. inlet die	$12 \times 45$
2. converging die	$12 \times 18 + 15 \times 8$
3. land region	$15 \times 12 + 20 \times 12$
4. draw-down region	$20 \times 25$
5. coating region	$20 \times 25$

**Table IV.**  
Tube-tooling; mesh  
characteristics, sub-  
region zones



(a) pressure contours



(b)  $I_2$  contours

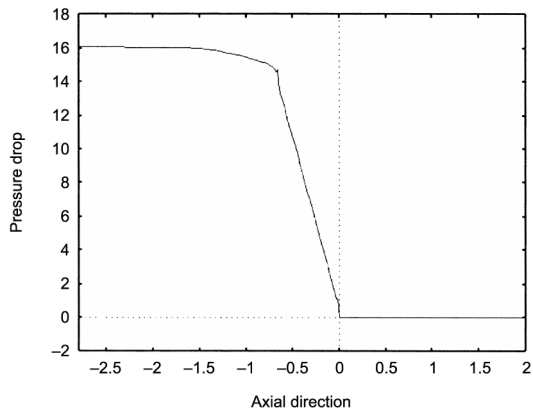


(c)  $\epsilon$  contours

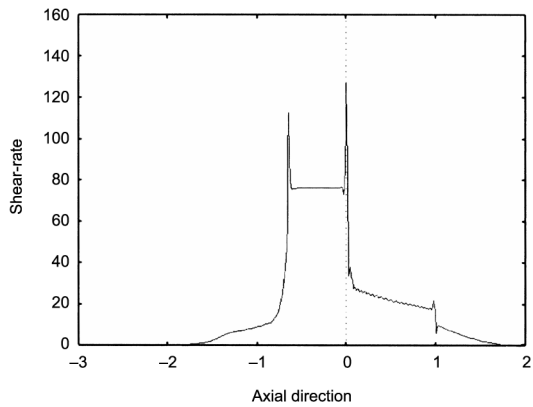
**Figure 16.**  
Tube-tooling: (a) pressure contours, (b)  $I_2$  contours, (c)  $\epsilon$  contours

section, followed by a sharp decline when the polymer meets the wire. Traveling with the wire, the rate of decrease in shear-rates is minimal. The final shear-rates, taken up at the end of the coating, are about 0.26 and 1.0 units for bottom and top surfaces, respectively.

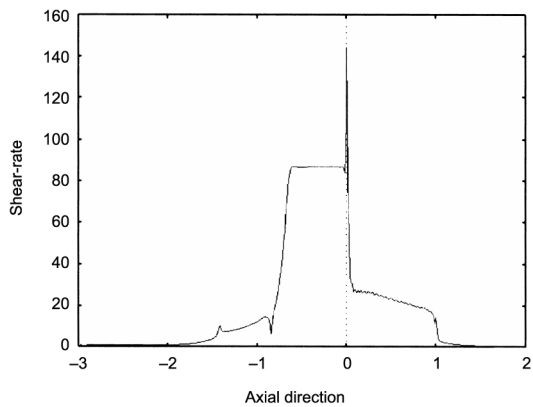
The state of strain-rate  $\epsilon$  is illustrated in Figure 16c. This quantity is significant in the converging tube. It reaches a maximum of about 4.43 units, an order of magnitude lower than that for shear-rate maxima. This is a fifth of that corresponding to pressure-tooling maxima. Large values of strain-rate are also located, of less magnitude, at the start of the draw-down section just beyond the die-exit. The value reached is about 2.50 units, half of that observed in the converging die-cone. The profiles for  $\epsilon$  along the axial direction, for top and bottom surfaces show similar behaviour to each other, with exceptions at the sharp adjustments in geometry. Elongation-rates are large at the land region



(a) pressure along the wire



(b)  $I_2$  on top surface

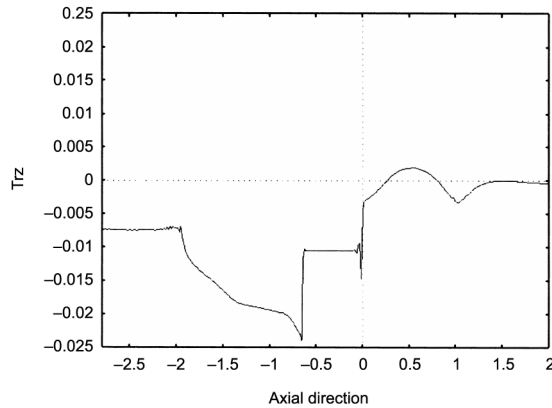


(c)  $I_2$  on wire

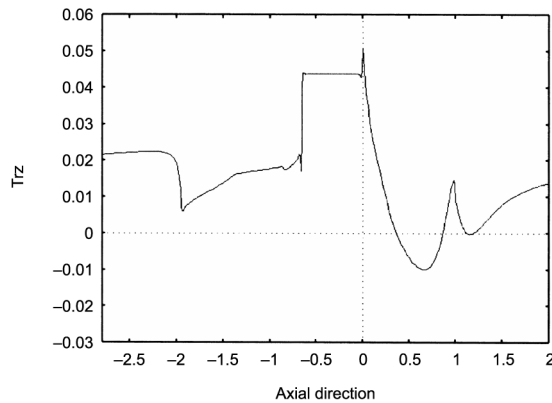
**Figure 17.**  
Tube-tooling: (a) pressure  
along the wire, (b)  $I_2$  on  
top surface, (c)  $I_2$  on  
bottom surface

entrance, reaching a maximum of 4.43 units, being minimal in the remaining flow section. Shear and strain-rates are important measurable quantities that describe the state of flow and, according to the ranges encountered, may explain the polymer response to different flow scenarios.

Component stress profiles along the top surface are provided in Figure 18 a) for  $\tau_{rz}$  and b) for  $\tau_{zz}$ . One may observe from this, that along the inlet-tube,  $\tau_{zz}$  is constant, of about 0.02 units. Sudden change occurs with each adjustment in geometry. An increase of  $\tau_{zz}$  is observed within the converging cone of the die, reaching a value of 0.045 units at the entrance to the land-region.  $\tau_{zz}$  is constant over the land-region, followed by a sudden increase due to singularity, where the polymer departs from the die to the draw-down section. A sharp decrease within the draw-down is generated. When the polymer makes contact with the wire,  $\tau_{zz}$  increases providing a residual stress of about 0.012 units. In contrast,



(a)  $T_{rz}$



(b)  $T_{zz}$

**Figure 18.**  
Tube-tooling: on top  
surface (a)  $T_{rz}$  (b)  $T_{zz}$

the shear-stress  $\tau_{rz}$  is lower in value than the  $\tau_{zz}$  component, as displayed in Figure 18a.  $\tau_{rz}$  starts with a value of about 0.007 units at the inlet tube, increase over the converging cone to reach a constant value of 0.01 units across the land-region. Subsequently,  $\tau_{rz}$  decreases in the draw-down and coating regions to a minimum value less than 0.001 units. Contours are plotted in Figure 19 to analyse the state of stress over the whole domain and in various components.  $\tau_{rr}$  can be considered to be small in the inlet-tube and land-region: it is significant in the converging cone, draw-down and coating regions. A maximum of about 0.05 units is realised in the draw-down section. For  $\tau_{rz}$ , we observe a peak (0.024 units) in the converging die-cone, near the entrance to the land-region. The shear-stress is also prominent in the land-region, but of less magnitude (about half) than that over the converging cone. Axial  $\tau_{zz}$  stress is most significant in the land-region, as observed in Figure 19c. The maximum

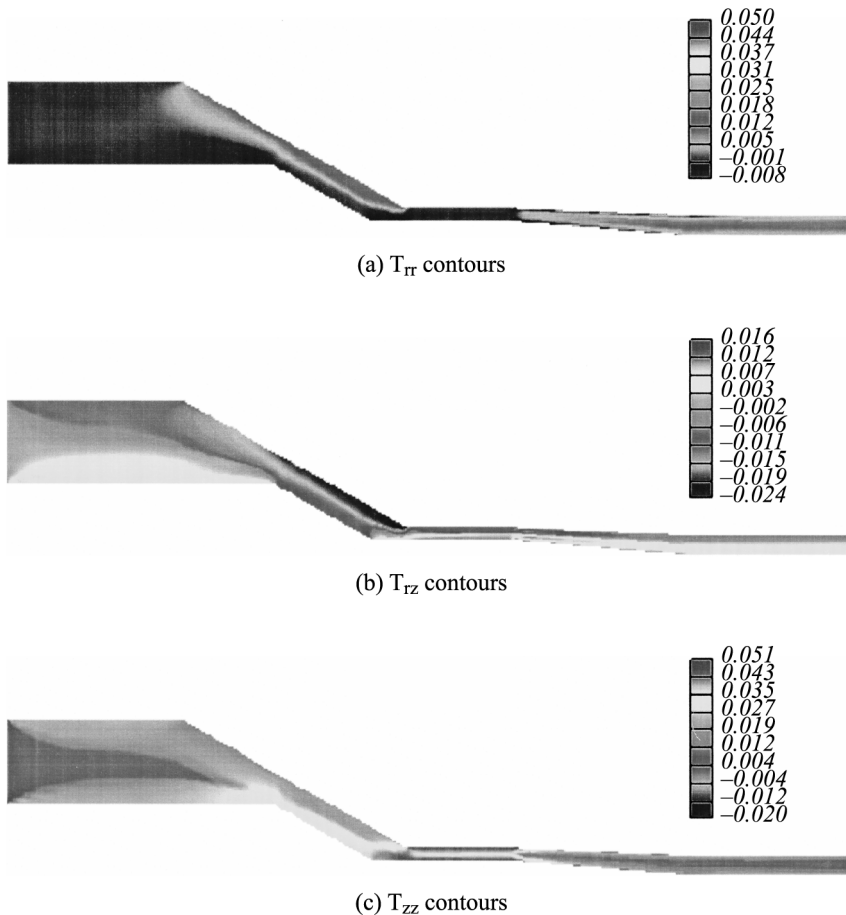


**Figure 19.**  
Tube-tooling: (a)  $T_{rr}$   
contours, (b)  $T_{rz}$   
contours, (c)  $T_{zz}$  contours

value, 0.051 units, is double that of the shear-stress. Hence, *residual stressing* to the coating is dominated by the axial component.

6.4 Parallel timings

Parallel computation is employed, within the simulations performed through a spatial domain decomposition method. The domain of interest is decomposed into a number of subdomains, according to available resources and total number of DOF. In this study, uniform load distribution is ensured using a Recursive Spectral Bisection method (Simon, 1991). Though the method is quite general, uniform load may be organized if domain subdivision is straightforward, otherwise loading will be approximately uniform, from which manual adjustment may be made. As the short-die domain has relatively few DOF, the domain is decomposed into instances with only two and four subdomains. In contrast, tube-tooling and pressure-tooling domains are partitioned into as many as eight sub-domains.

In Table V, information is presented on domain decomposition, the number of elements and nodes per subdomain, the number of interfacing nodes and ratio of subdomain nodes to interfacing nodes ( $C_n = N_n : I_{nn}$ ). With an increasing number of subdomains, interfacing nodes ( $I_{nn}$ ) increase (as does communication cost), whilst the number of elements, nodes ( $N_n$ ) and degrees-of-freedom per subdomain decreases.

Parallel timings are generated on a networked cluster of single processor Intel 450 MHz Solaris workstations, a distributed-memory homogeneous platform. A public domain PVM 3.4.3 version for message passing protocol has been employed to support interprocessor communication through networking with fast 100 Mbit/s EtherNet. Computed results are presented through the

Domain	Elements/ subdomain	Nodes/ subdomain	Interface nodes		$C_n$	
			Master	Slave	Master	Slave
Short-die						
1	288	377	–	–	–	–
2	144	325	13	13	4%	4%
4	72	169	39	26	23%	15.4%
Pressure-tooling						
1	3810	7905	–	–	–	–
2	1905	3968	31	31	0.78%	0.78%
4	953	1976	93	62	4.71	3.14%
8	476	988	217	62	22.0%	6.28%
Tube-tooling						
1	4714	9755	–	–	–	–
2	2357	4878	31	31	0.64%	2.75%
4	1178	2439	103	67	4.22%	2.75%
8	589	1222	272	71	22.3%	5.81%

**Table V.**  
Domain  
decomposition data

parallel performance of the Taylor-Galerkin scheme, by measuring metrics of speed-up and efficiency, with increasing numbers of processors (hence, sub-tasks). The total speed-up ( $S_n$ ) factor and efficiency ( $\eta_n$ ) are defined as:

$$S_n = \frac{T_{\text{seq}}}{T_n}, \quad \eta_n = \frac{S_n}{n},$$

Where  $n$  is the number of processors,  $T_{\text{seq}}$  is the CPU time in seconds (s) for the sequential algorithm and  $T_n$  is the CPU time for the parallel algorithm. CPU time  $T_n$  of the parallel computation can be decomposed into computation time ( $T_n^{\text{comp}}$ ) and communication time ( $T_n^{\text{comm}}$ ). Timings correspond to total job run-time, inclusive of input-output and communication latency.

In Table VI, speed-up and efficiency factors are tabulated for our parallel implementations. Speed-up is plotted in Figure 20 for the viscoelastic simulations if short-die, tube-tooling and pressure-tooling problems, with increasing numbers of processors. As the short-die problem has fewer DOF, eight percent loss of efficiency is observed with up to four processors. For two-subdomains,

Processors	Short-die		Pressure-tooling		Tube-tooling	
	$S_n$	$\eta_n$	$S_n$	$\eta_n$	$S_n$	$\eta_n$
1	1.00	1.00	1.00	1.00	1.00	1.00
2	1.94	0.97	1.99	0.99	1.99	0.99
4	3.66	0.92	3.98	0.99	3.99	0.99
8	–	–	7.44	0.93	7.61	0.95

**Table VI.**  
Parallel speed-up  
and efficiency

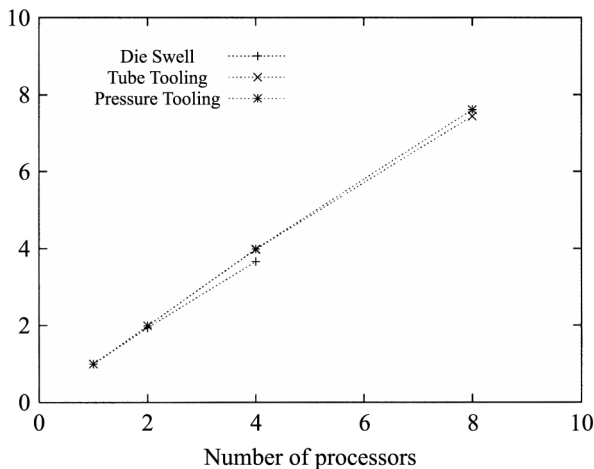


**Figure 20.**  
Parallel speed-up

the master processor has to communicate with thirteen interfacing nodes. Moving to four-subdomains, the size of each task on a slave processor halves. For full pressure-tooling and tube-tooling, with two and four subdomains, the ratio between computation and communication remains small. At eight subdomains, this ratio is of the same order as that for the short-die problem and four processor. Under such circumstances with tube-tooling, the parallel algorithm loses five percent efficiency and seven percent for pressure-tooling problems. The consequence of this is felt within our parallel implementation via the ratio of internal to boundary nodes in each instance. This ratio will affect the proportion of cost, split between communication and sub-problem computation (hence, the masking of communication (Baloch *et al.*, 2000; Grant *et al.*, 1998)).

In Table V, we have recorded data relating to interfacing nodes and the ratio between subdomain nodes and interfacing nodes ( $C_n$ ). For the short-die with two slave processors, the number of nodes is relatively few and  $C_n$  is around four percent. Therefore, we immediately lose efficiency of about three percent. The loss is even greater with four slave processors, see Table VI. Such efficiency loss diminishes as  $C_n$  decreases, as clearly demonstrated in both pressure-tooling and tube-tooling instances. To take full advantage of parallelism and gain optimal performance levels, we seek to increase problem size and select a minimal  $C_n$  ratio, through a judicious choice of domain subdivision (sub-task generation, demanding prerequisite slave processors). For both pressure-tooling and tube-tooling problems and up to four slave processors, the  $C_n$  ratio is about three percent and we lose efficiency of one percent. At eight slave processors, the parallel implementation loses seven percent efficiency for the pressure-tooling problem, and five percent for the tube-tooling problem. To achieve optimal performance levels, we must ensure a balance between the number of processors and total number of degrees-of-freedom per subdomain. This will also provide the optimal ratio between ( $T_n^{\text{comm}}$ ) and  $T_n^{\text{comp}}$  times. We recognize that communication and computation times relate to different hardware mechanisms. One may identify an acceptable threshold level on efficiency loss, of say up to five percent. For the present study, this would imply the efficient use of two slave-processors for the short-die problem, four slave-processors for pressure-tooling and eight slave-processors for tube-tooling. With the proviso of sufficient processors, larger problems may be tackled in this manner.

## 7. Conclusions

In the case of *short-die pressure-tooling* flow, there was no melt-wire sudden contact and smooth solutions were established on the wire at the die-exit. For the full-die study in contrast to the short-die, ranges of shear rise ten-fold and extension rate by one hundred times. For dimensional equivalents, one must scale by  $O(10^3)$ . For the *short-die tooling*, the major observations are: maximum

shear rates arise at die-exit, top-surface, whilst for extension rates they lie within the free-jet region. The corresponding situation for strain rates is more marked, but displaying similar trends to shear rate. Axial stress maxima occur at the top surface on die-exit. For *full-die pressure-tooling*, shear rate maxima on the top surface occur over the land-region, and in particular, peak at the die-exit. The level is some fifteen times larger than that for the short-die. Shear rate maxima on the wire are lower than that at the top surface, by a factor of three. The double (sudden shock) peaks in shear rate at the bottom surface for full-die flow, do not appear in the short-die case. These are a new feature, introduced as a consequence of the full-die and melt-wire contact. There is a double peak along the wire, with the die-exit value being marginally larger than that at melt-wire contact. Extension rate maxima are lower than shear rates by one order, but have increased one hundred fold from the short-die case. Extension rates peak at the melt-wire contact and across land/die-exit region. The maximum corresponds to the die-exit. The pressure drop across the flow is almost entirely confined to the land-region, and is magnified some twenty-two times over that for the short-die. The behaviour in stress for full-tooling reveals the “shock impact” as the fluid makes contact with the wire. The largest axial stress arises at the melt-wire contact point. The swelling ratios for the EPTT models are 15 per cent higher than that observed for short-die tooling. Hence, the influence of the die flow itself is exposed. The adequacy of the free-surface procedures is also commended.

In contrast, focusing on *tube-tooling* desing, stress and pressure build-up is realised in the land-region section, as with pressure-tooling. The principal stress component  $\tau_{zz}$  is significant at the end of the coating, generating a residual stress of about 0.012 units and vanishing shear-stress. This is similar to pressure-tooling. Shear-rates are of  $O(10^2)$  units, reaching a maximum of 144 units, a quarter of that corresponding to the pressure-tooling problem. This maximum is observed at the exit of the die. Tube-tooling strain-rates are an order of magnitude lower than tube-tooling shear-rates: strain-rate maxima reach 4.43 units, again one quarter of those for pressure-tooling. Largest strain-rates are generated throughout the converging did-tube, with lesser values in the draw-down section (extrudate). Such elements of variation between designs would have considerable impact upon the processes involved.

Distributed parallel processing has been shown to be an effective computational tool to simulate industrial wire-coating flows. Ideal linear speed-up in run-times has been extracted, based on the number of processors utilised. Increasing the size of the problem, would render even greater efficiency, providing a wider pool of processors were made available.

## References

- Baloch, A. and Webster, M.F. (1995), “A computer simulation of complex flows of fibre suspensions”, *Computers Fluids*, 24 No. 2, pp. 135-51.

- Baloch, A, Grant, P.W. and Webster, M.F. (2000), Homogeneous and heterogeneous distributed cluster processing for two and three-dimensional viscoelastic flows, submitted to *Int. J. Num. Meth. Fluids*, available as CSR 16.
- Baloch, A., Townsend, P. and Webster, M.F. (1998), "On the highly elastic flows", *J. Non-Newtonian Fluid Mech.*, 75, pp. 139-66.
- Binding, D.M., Blythe, A.R., Gunter, S., Mosquera, A.A., Townsend, P. and Webster, M.F. (1996), "Modelling Polymer Melt Flows in Wire Coating Processes", *J. non-Newtonian Fluid Mech.*, 64, pp. 191-209.
- Chung, T.S. (1986), "The Effect of Melt Compressibility on a High-Speed Wire-Coating Process", *Polym. Eng. Sci.*, 26 No. 6, pp. 410-4.
- Caswell, B. and Tanner, R.I. (1978), "Wire Coating Die Design Using Finite Element Methods", *J. Polym. Sci.*, 5, pp. 416-21.
- Crochet, M.J., Davies, A.R. and Wlalter, K. Numerical simulation of Non-Newtonian Flow, Rheology Series, 1, Elsevier Science Publishers, (1984).
- Carew, E.O.A., Townsend, P. and Webster, M.F. (1993), "A Taylor-Petrov-Galerkin Algorithm for Viscoelastic Flow", *J. Non-Newtonian Fluid Mech.*, 50, pp. 253-87.
- Grant, P.W., Webster, M.F. and Zhang, X. (1998), "Coarse Grain Parallel Simulation for Incompressible Flows", *Int. J. Num. Meth. Eng.*, 41, pp. 1321-37.
- Haas, K.U. and Skewis, F.H. (1974), "SPE ANTEC", *Tech. Paper*, 20, p. 8.
- Han, C.D. and Rao, D (1978), "Studies of Wire Coating Extrusion. I. The Rheology of Wire Coating Extrusion", *Polym. Eng. Sci.*, 18 No. 13, pp. 1019-29.
- Hawken, D.M., Tamaddon-Jahromi, H.R., Townsend, P. and Webster, M.F. (1990), "A Taylor-Galerkin-based algorithm for viscous incompressible flow", *Int. J. Num. Meth. Fluid*, 10, pp. 327-51.
- Mitsoulis, E. (1986), "Finite Element Analysis of Wire Coating", *Polym. Eng. Sci.*, 26 No. 2, pp. 171-86.
- Matallah, H., Townsend, P. and Webster, M.F. (1998), "Recovery and stress-splitting schemes for viscoelastic flows", *J. Non-Newtonian Fluid Mech.*, 75, pp. 139-66.
- Matallah, H., Townsend, P. and Webster, M.F. (2000), Viscoelastic Computations of Polymeric Wire-Coating Flows, *Int. J. Num. Meth. Heat Fluid Flow*, accepted for publication 2001, available as CSR 13, University of Wales, Swansea.
- Matallah, H., Townsend, P. and Webster, M.F. (2000), "Viscoelastic Multi-Mode Simulations of Wire-Coating", *J. Non-Newtonian Fluid Mech.*, 90, pp. 217-41.
- Mitsoulis, E., Wagner, R. and Heng, F.L. (1988), "Numerical Simulation of Wire-Coating Low-Density Polyethylene: Theory and Experiments", *Polym. Eng. Sci.*, 28 No. 5, pp. 291-310.
- Mutlu, I., Townsend, P. and Webster, M.F. (1998a), "Computation of Viscoelastic Cable Coating Flows", *Int. J. Num. Meth. Fluids*, 26, pp. 697-712.
- Mutlu, I, Townsend, P. and Webster, M.F. (1998b), "Simulation of Cable-Coating Viscoelastic Flows with Coupled and Decoupled Schemes", *J. Non-Newtonian Fluid Mech.*, 74, pp. 1-23.
- Ngamaramvaranggul, V. (2000), Numerical Simulation of Non-Newtonian Free Surface Flows PhD thesis University of Wales, Swansea.
- Ngamaramvaranggul, V. and Webster, M.F. (2000a), "Simulation of Coatings Flows with Slip Effects", *Int. J. Num. Meth. Fluids*, 33, pp. 961-92.
- Ngamaramvaranggul, V. and Webster, M.F. (2000b), "Computation of Free Surface Flows with a Taylor-Galerkin/Pressure-Correction Algorithm", *Int. J. Num. Meth. Fluids*, 33, pp. 993-1026.

- 
- Ngamaramvaranggul, V. and Webster, M.F. (2001), "Viscoelastic Simulation of Stick-Slip and Die-Swell Flows", *Int. J. Num. Meth. Fluids*, 36, pp. 539-95.
- Ngamaramvaranggul, V. and Webster, M.F. (2002), "Simulation of Pressure-Tooling Wire-Coating Flow with Phan-Thien/Tanner Models", *Int. J. Num. Meth. Fluids*, 38, pp. 677-710.
- Phan-Thien, N. (1978), "A Non-linear Network Viscoelastic Model", *J. Rheol.*, 22, pp. 259-83.
- Phan-Thien, N. and Tanner, R.I. (1977), "A New Constitutive Equation Derived from Network Theory", *J. Non-Newtonian Fluid Mech.*, 2, pp. 353-65.
- Phan-Thien, N. and Tanner, R.I. (1992), Boundary-Element Analysis of Forming Processes in 'Numerical Modelling of Material Deformation Processes: Research, Development and Application' by P. Hartley, I. Pillinger and C. Sturgess (Eds), Springer-Verlag, London.
- Pittman, J.F.T. and Rashid, K. (1986), "Numerical Analysis of High-Speed Wire Coating", *Plast. Rub. Proc. Appl.*, 6, pp. 153.
- Richardson, S. (1970), "A stick-slip problem related to the motion of a free jet at low Reynolds numbers", *Proc. Camb. Phil. Soc.*, 67, pp. 477-89.
- Simon, H.D. (1991), "Partitioning of unstructured problems for parallel processing", *Computer Systems in Engineering*, 2, pp. 135-48.
- Tadmor, Z. and Bird, R.B. (1974), "Rheological Analysis of Stabilizing Forces in Wire-Coating Die", *Polym. Eng. Sci.*, 14 No. 2, pp. 124-36.
- Tanner, R.I. (1985), *Engineering Rheology*, Oxford University Press, London.
- Townsend, P. and Webster, M.F. (1987), An algorithm for the three-dimensional transient simulation of non-Newtonian fluid flows, in G. Pamde, J. Middleton (Eds.), Proc. Int. Conf. Num. Meth. Eng.: Theory and Applications, NUMETA, Nijhoff, Dordrecht, pp. T12/1-11.
- Wagner, R. and Mitsoulis, E. (1985), *Adv. Polym. Tech.*, 5, pp. 305.